EDGE ARTICLE

Interfacial polarization enables dual pathways for electrosynthesis of propyl acetate

Xichang Liu,†[a] Yimin Jiang,†[a] Wei Chen, [ID][a] Jixiang Wu,[a] Yongmin He, [ID][a] Yu-Cheng Huang,[b] Ying-Rui Lu,[c] Yansong Zhou [ID] *[a] and Shuangyin Wang [ID] *[a]

The direct electrosynthesis of value-added esters from carbon monoxide (CO) represents a promising strategy for sustainable carbon utilization. In this study, we report the synthesis of propyl acetate with a faradaic efficiency of 16.5% and a partial current density reaching up to 24.7 mA cm^{-2} *via* CO electrolysis on a polarized Cu/Cu$_3$N interface. Comprehensive mechanistic investigations elucidate a dual-pathway mechanism: ketene undergoes nucleophilic addition with *n*-propanol; and C$_2$–C$_3$ coupling occurs between nucleophilic *CH$_2$CO and electrophilic intermediates such as *COHCOCO. Charge redistribution and interfacial polarization induced by the Cu/Cu$_3$N interface reduce the activation barrier for the electrophilic addition between C$_2$–C$_3$ intermediates. These findings offer an alternative and sustainable pathway for the synthesis of esters through direct CO electroreduction.

Introduction

Carbon monoxide (CO), which can be efficiently derived from carbon dioxide (CO$_2$) *via* well-established electrochemical or thermochemical methods, is a key intermediate for multi-carbon product formation in electrocatalytic CO$_2$/CO conversion processes.[1,2] However, the current multi-carbon products from electrochemical CO reduction are mainly limited to acetate, ethylene, ethanol, and *n*-propanol.[3] The synthesis of other high-value products, such as esters, is highly desirable from both practical and theoretical perspectives.

Among the products of electrocatalytic CO reduction reaction (CORR), esters are particularly attractive due to their wide applications in fragrances, solvents, *etc.* Of these, propyl acetate, valued for its low toxicity, excellent solvency, and biocompatible characteristics, has been widely utilized in coatings, pharmaceuticals and biomedical fields.[4] Given these diverse applications, global demand for propyl acetate is growing. Market research estimates its value at USD 1.56 billion in 2024, projected to reach USD 2.54 billion by 2034 with a compound annual growth rate of 4.98%, reflecting its expanding role across multiple sectors.[5]

Traditionally, propyl acetate is synthesized through the esterification of acetic acid with *n*-propanol, requiring harsh

reaction conditions (363–403 K, >1 atm), corrosive acid catalysts, and energy-intensive purification procedures.[6] CORR offers a sustainable alternative under ambient conditions, utilizing electricity as the driving force. This approach reduces carbon emissions and simplifies synthesis by integrating CO conversion and ester formation into a single step (Fig. 1). The realization of the electrosynthesis of esters in our previous work *via* CORR encourages us to develop an alternative sustainable pathway for propyl acetate production.[7] However, selective production of propyl acetate *via* CORR remains a significant challenge, primarily due to the difficulty and complexity involved in the formation of C$_2$/C$_3$ intermediates.[8,9] Efficient catalysts and mechanistic insights are essential to improve propyl acetate selectivity and yield.

Propyl acetate production *via* CORR involves the sequential formation of three C–C bonds and one C–O bond. Copper-based catalysts can achieve this goal by optimally adsorbing key intermediates, thus promoting C–C bond formation.[7] A Cu/Cu$^{\delta+}$ mixed valence system has been shown to effectively promote the C–C coupling process.[10–12] However, Cu$^{\delta+}$ species derived from oxides are prone to reduction to metallic Cu under cathodic potentials.[13] To address this challenge, strategies including introducing heteroatoms to form compounds such as copper oxides, borides, and nitrides have been developed to stabilize Cu$^{\delta+}$ during CO$_{(2)}$RR.[14–16] Among these, copper nitride (Cu$_3$N) stands out due to its Cu–N bond maintained at the reductive potentials, thereby providing stable Cu$^{\delta+}$ sites during CO$_{(2)}$RR.[17,18] Moreover, recent studies indicate that Cu–N-based catalysts can enhance the stabilization of C$_3$ intermediates, which may promote propyl acetate formation pathways.[19]

Herein, we report the electrosynthesis of a substantial amount of propyl acetate *via* CORR on a Cu/Cu$_3$N

[a]State Key Laboratory of Chemo and Biosensing, College of Chemistry and Chemical Engineering, Advanced Catalytic Engineering Research Center of the Ministry of Education, Hunan University, Changsha, China

[b]Curtin Centre for Advanced Energy Materials and Technologies, WA School of Mines: Minerals, Energy and Chemical Engineering (WASM-MECE), Curtin University, Perth WA 6102, Australia

[c]National Synchrotron Radiation Research Center, Hsinchu 300092, Taiwan

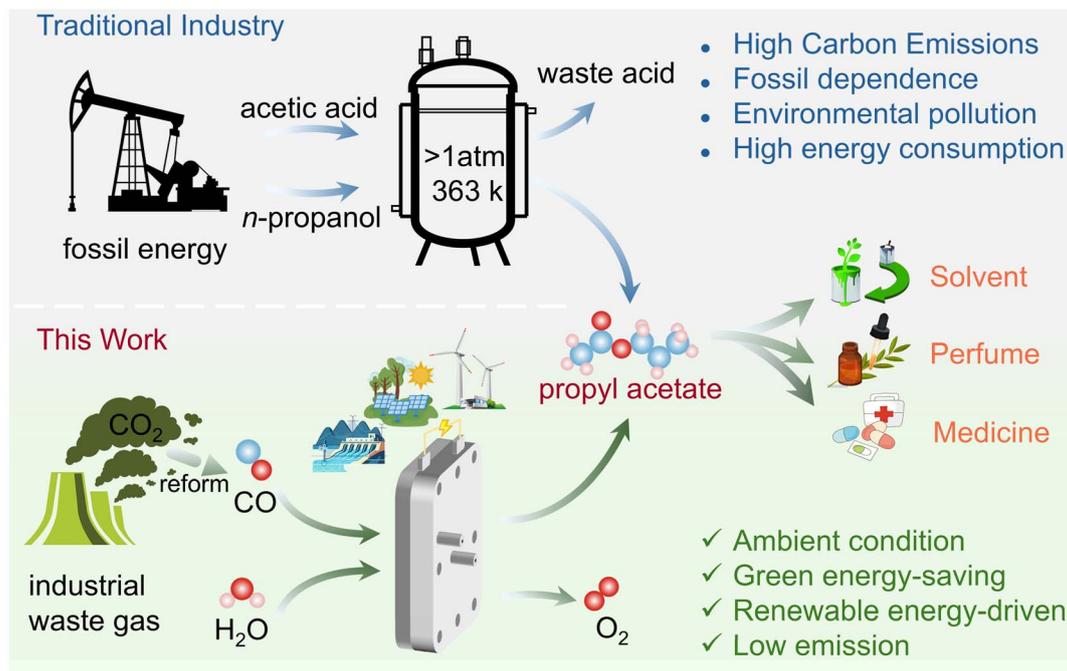† These authors contributed equally to this work.

Fig. 1 Comparison between traditional and electrochemical synthesis of propyl acetate.

electrocatalyst. The integration of Cu_3N onto metallic Cu generates coherent interfaces that modulate the electronic structure and stabilize key intermediates, thereby promoting C–C and C–O bond coupling for propyl acetate production. The Cu/Cu_3N catalyst achieves a considerable production of propyl acetate with a faradaic efficiency (FE) of 16.5% and a partial current density reaching up to 24.7 mA cm^{-2}—approximately an order of magnitude higher than the previously reported value.[7] A dual-pathway mechanism for propyl acetate formation is proposed. Beyond the *n*-propanol–ketene (CH_2=C=O) addition reaction, we identify parallel C_2–C_3 intermediate coupling pathways involving *CH_2CO and active C_3 intermediates (*e.g.*, *COHCOCO). These findings are supported by both experimental and theoretical results.

Results and discussion

Mechanistic motivation and structural insights

Two possible interfacial configurations exist between Cu and Cu_3N phases: vertically stacked (Cu/Cu_3N) and laterally connected (Cu–Cu_3N). Projected density of states (PDOS) analysis indicates that the polarized Cu sites in both configurations exhibit stronger orbital interactions between C_{2p} states of the *CO compared to those on the pristine Cu surface (Fig. S1). This enhanced interaction is expected to promote the coupling of *CO, thereby enhancing the preferential generation of multi-carbon species during CORR to promote propyl acetate formation.[15,20]

Guided by these insights, we synthesized the Cu/Cu_3N electrocatalyst by electrochemically deriving it from N_2 plasma-treated basic copper nitrate ($Cu_2(OH)_3NO_3$, BCN). Both the as-prepared BCN and the N_2 plasma-treated BCN (p-BCN)

samples exhibit the monoclinic $Cu_2(OH)_3NO_3$ phase (JCPDS no. 75-1779, Fig. 2a).[21] Compared to the X-ray diffraction (XRD) pattern of BCN, the shifts of the characteristic (001) and (002) planes observed for p-BCN may be attributed to the formation of surface/interfacial heterostructures during N_2 plasma treatment (Fig. S2). The scanning electron microscopy (SEM) analysis reveals the formation of dense nanoparticles with a size of approximately 10 nm on the surface of bulk BCN particles in the p-BCN sample, confirming the formation of a new surface phase with N_2 plasma treatment (Fig. S3). X-ray photoelectron spectroscopy (XPS) reveals the coexistence of reduced Cu^{2+} species (Cu^+ and/or Cu^0) with Cu^{2+} (Fig. S4), suggesting the partial reduction of Cu^{2+} induced by N_2 plasma treatment. The Cu LMM Auger spectrum further confirms that the reduced Cu^{2+} species are predominantly Cu^+ species (Fig. 2b).[22] In the N 1s spectrum of p-BCN (Fig. 2c), peaks attributed to nitrogen vacancies and the Cu–N bond in copper nitrides are observed, suggesting the formation of a N_2 plasma treatment induced copper nitride phase on the BCN surface.[19,23] In the transmission electron microscopy (TEM) image of p-BCN, lattice spacings of 0.220 nm and 0.269 nm, assigned to the (111) and (110) planes of Cu_3N, were observed, confirming that the surface copper nitride phase is Cu_3N.[24,25] This is further supported by the results of Raman spectroscopy analysis in which the characteristic band of Cu_3N at 660 cm^{-1} was observed (Fig. 2d and S5).[26] High-angle annular dark-field scanning transmission electron microscopy (HAADF-STEM) and energy-dispersive X-ray (EDX) spectroscopy mapping further confirm the homogeneous distribution of Cu, N, and O throughout the p-BCN sample (Fig. 2e and f). In summary, these results demonstrate the successful introduction of Cu_3N onto the $Cu_2(OH)_3NO_3$ surface for the subsequent electrochemical
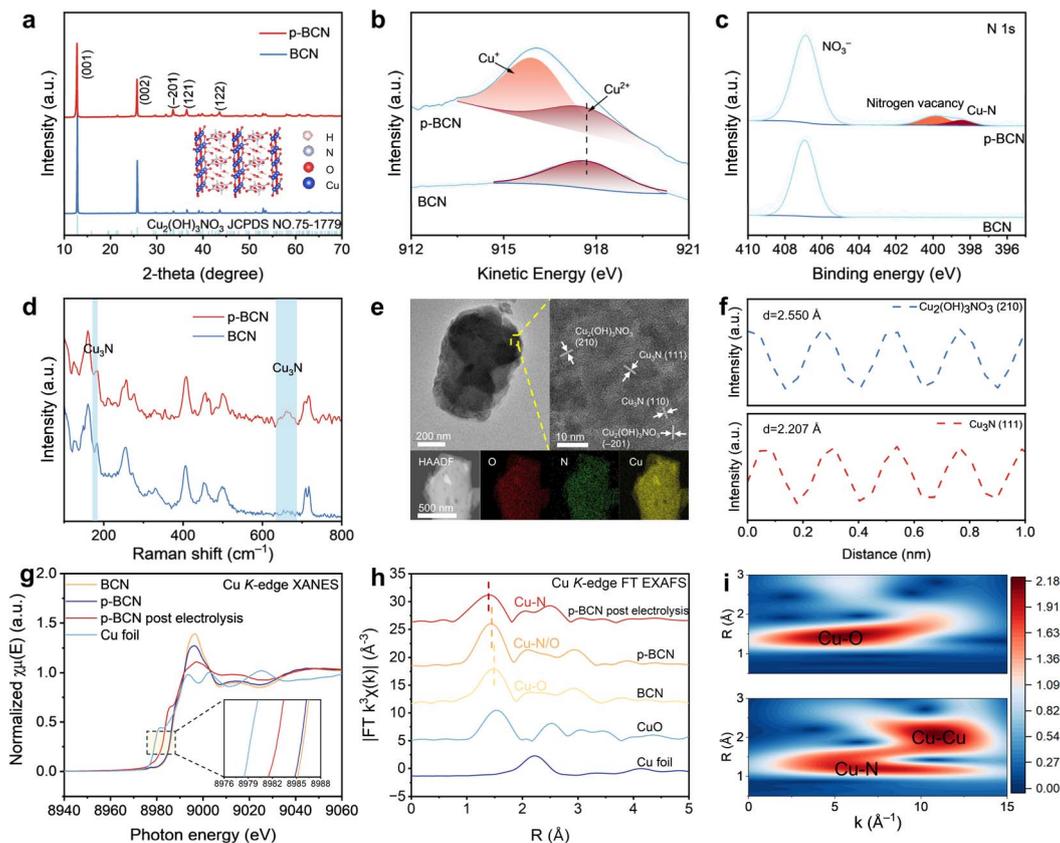
Fig. 2 Structural and electronic characterization of the catalysts. (a) XRD patterns of BCN and p-BCN. (b) Cu LMM Auger spectra of BCN and p-BCN. (c) XPS N 1s spectra of BCN and p-BCN. (d) Raman spectra of BCN and p-BCN. (e) TEM, HRTEM image and HAADF-STEM image of p-BCN, along with the corresponding EDX elemental mapping images. (f) Integrated pixel intensities extracted from the HRTEM images of BCN and p-BCN. (g) Normalized Cu K-edge X-ray absorption near-edge structure (XANES) spectra of the catalysts. (h) Fourier-transformed extended X-ray absorption fine structure (EXAFS) spectra at the Cu K-edge. (i) Wavelet transform (WT) of the k^3-weighted Cu K-edge EXAFS spectra.

derivation of Cu/Cu$_3$N electrocatalysts. Moreover, the relative amount of Cu$_3$N present on the catalyst surface was quantitatively estimated from the XPS N 1s spectra (Table S1). X-ray absorption spectroscopy was used to investigate the local atomic structure and valence electronic structure of the catalysts. The Cu K-edge X-ray absorption near-edge structure (XANES) spectra indicate that the oxidation state of Cu in p-BCN is slightly lower than that in BCN (Fig. 2g). This trend is consistent with the XPS results, indicating that N$_2$ plasma treatment leads to the formation of reduced Cu species.[27] The further pronounced shift of the absorption edge in the Cu K-edge spectrum of p-BCN after post-electrolysis indicates the reduction of the Cu$_2$(OH)$_3$NO$_3$ phase under CORR conditions (Fig. 2g). The Fourier-transformed (FT) k^3-weighted extended X-ray absorption fine structure (EXAFS) spectra of Cu reveal changes in the local coordination environment (Fig. 2h). Specifically, in BCN, the first-shell coordination bond length is 1.53 Å, corresponding to the Cu–O bond. In p-BCN, this bond length shortens to 1.46 Å due to the co-existence of the Cu–N bond and Cu–O bond. Notably, after electrolysis, the bond length shifts to 1.41 Å, which is attributed to the disappearance of Cu–O coordination and the dominance of the Cu–N bond.[25,28] This result is further supported by wavelet-transformed (WT) k^3-

weighted EXAFS analysis (Fig. 2i), indicating the stable presence of Cu$_3$N alongside the reduction of BCN under CORR conditions. Together with the results from XPS, Raman, and TEM analyses of the post-reacted samples, it is clearly indicated that the Cu–N bond associated with Cu$_3$N can be stably retained, in contrast to the complete reduction of Cu$_2$(OH)$_3$NO$_3$ to metallic Cu (Fig. S6 and S7). Collectively, these findings confirm the successful formation and structural stability of the Cu/Cu$_3$N interface derived from p-BCN during CO$_2$RR.

Catalytic performances toward propyl acetate production

We initially assess the potential of p-BCN derived Cu/Cu$_3$N for CORR. Linear sweep voltammetry (LSV) tests conducted in both N$_2$- and CO-saturated electrolytes showed a distinct higher current density under CO-saturated conditions, underscoring its higher CORR preference over the competing hydrogen evolution reaction. Moreover, p-BCN derived electrocatalysts demonstrated a more positive onset potential and higher current density compared to that derived from BCN, indicating its improved reaction kinetics and enhanced catalytic performance for CORR (Fig. S8).[29] In situ electrochemical impedance spectroscopy (EIS) combined with distribution of relaxation times (DRT) analysis was conducted, providing evidence of
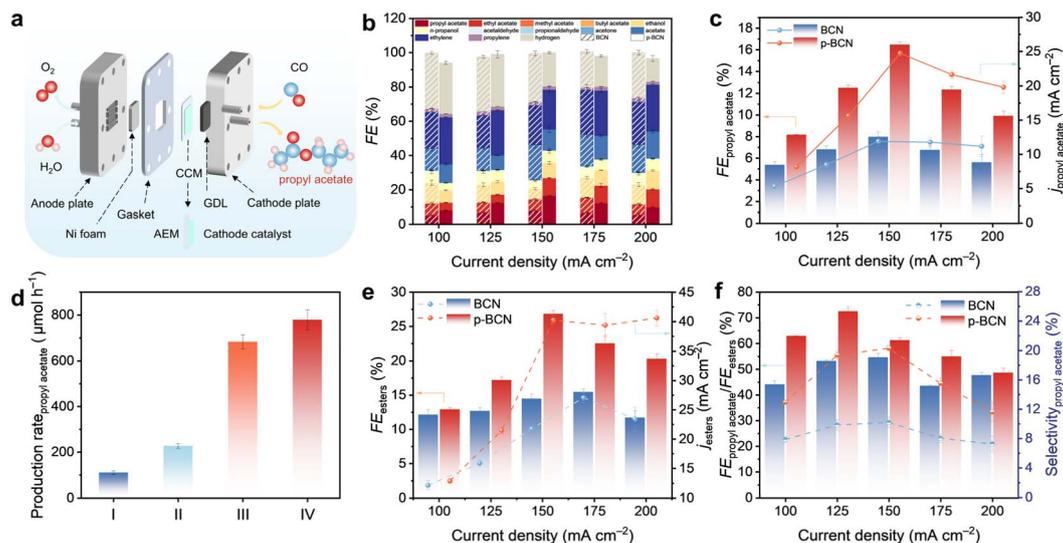
Fig. 3 Electrocatalytic performances of BCN-derived and p-BCN-derived electrocatalysts. (a) Schematic illustration of electrochemical CO reduction to propyl acetate in a MEA system. (b) FE of CO reduction products at various current densities. (c) FE and partial current density of propyl acetate. (d) Propyl acetate production rate with different feedstocks and catalysts: (I and II) CO as a feedstock with the BCN-derived catalyst and p-BCN-derived catalyst, respectively. (III) co-feeding CO and n-propanol with the p-BCN-derived catalyst. (IV) co-feeding CO and n-propanol at the optimal gas–liquid mixture ratio with the p-BCN-derived catalyst. (e) FE and partial current density of ester products. (f) Selectivity of propyl acetate among ester products and total products at different current densities. Error bars correspond to the standard deviations of at least three independent measurements.

enhanced charge transfer efficiency and intrinsic catalytic kinetics.[30,31] (Fig. S9). These results collectively demonstrate p-BCN derived Cu/Cu$_3$N as a highly CORR catalyst.

We investigated the CORR performance of the catalysts in a membrane electrode assembly (MEA) system (Fig. 3a). p-BCN derived Cu/Cu$_3$N exhibited significantly enhanced CORR selectivity (Fig. 3b and Tables S2 and S3). At a current density of 150 mA cm^{-2}, the FE for C$_{2+}$ products increased from 71.5% to 80.6%. Notably, the BCN-derived catalyst demonstrated its outstanding advantages in the electrosynthesis of propyl acetate from CORR with a maximum FE of propyl acetate (FE$_{propyl\ acetate}$) of 8.0%, approximately four times higher than previously reported values.[7] On the p-BCN-derived catalyst, this value was further enhanced to a maximum FE$_{propyl\ acetate}$ of 16.5%, with the corresponding propyl acetate partial current density ($j_{propyl\ acetate}$) reaching up to 24.7 mA cm^{-2}, both of which are record values to date (Fig. 3c and S10–S13). To further identify the origin of the enhanced catalytic performance, two control samples—pristine Cu$_2$O and Ar-plasma-treated BCN (Ar-BCN)—were prepared and evaluated under identical CORR conditions (Fig. S14–S16). The results show that (i) the isolated Cu$_2$O phase exhibits negligible selectivity toward propyl acetate, and (ii) depositing Cu$_2$O onto the BCN surface does not improve propyl acetate selectivity. These findings indicate that the marked increase in propyl acetate selectivity cannot be attributed to residual Cu$_2$O species on the p-BCN surface. This confirms that the Cu/Cu$_3$N interface derived from p-BCN plays a decisive role in enhancing the faradaic efficiency for propyl acetate (FE$_{propyl\ acetate}$).

We further assessed the practical potential of electrosynthesis of propyl acetate via CORR. Productivity was evaluated at a current density of 150 mA cm^{-2}. The p-BCN-derived catalyst

achieved a propyl acetate yield of 227 μmol h^{-1} in a MEA with a working area of 4 cm^2. Furthermore, co-feeding of CO and n-propanol—identified as a key intermediate in propyl acetate formation from CORR in a MEA[7]—into the MEA cell can significantly enhance the production rate of propyl acetate up to 682 μmol h^{-1}. Further optimization of the gas–liquid mixture ratio can increase the n-propanol concentration, resulting in an elevated production rate of 779 μmol h^{-1} (Fig. 3d). Based on these remarkable performance metrics, we evaluated the scalability and industrial feasibility of propyl acetate production via the CORR process. A preliminary techno-economic analysis was conducted, incorporating both electrolyzer capital costs and the costs associated with the downstream separation of liquid products (Fig. S17a).[32] The calculation results indicate that the production cost of one ton of propyl acetate via the proposed CORR route is \$1084.3, which is significantly lower than the reference price for the liquid product (\$1542.1), indicating a favourable plant-gate levelized cost and promising economic viability. Sensitivity analyses show that at electricity prices of \$0.01–0.02 kWh^{-1} and cell voltages of 2.0–3.0 V, most operating conditions allow economically viable electrosynthesis of propyl acetate (Fig. S17b). These findings underscore the substantial economic potential of CORR-based electrocatalytic production of propyl acetate.

Other ester products, including methyl acetate, ethyl acetate, and butyl acetate, were also detected in the product stream. For the p-BCN-derived catalyst, the total ester FE reached 26.8% with a partial current density of 40.2 mA cm^{-2} (Fig. 3e), among which propyl acetate accounted for 72.5% of ester FE and up to 20.3% of all CORR products (Fig. 3f). These results further

highlight the significant potential of the p-BCN-derived catalyst for selective propyl acetate production.

We then sought to investigate the underlying factors contributing to the enhanced CORR performance of p-BCN derived catalysts. Double-layer capacitance measurements indicated comparable electrochemical active surface area (ECSA) values of BCN (139 μF) and p-BCN (156 μF), implying that the enhanced selectivity of p-BCN toward propyl acetate arises from its improved intrinsic catalytic activity (Fig. S18a–e). Besides, p-BCN exhibited a 1.8-fold higher ECSA-normalized propyl acetate partial current density (Fig. S15f), demonstrating the superior catalytic capability of the Cu/Cu$_3$N heterojunction for selective propyl acetate production.

The reaction microenvironment critically dictates product selectivity in a MEA. The anion exchange membrane (AEM) thickness is found to play a pivotal role by modulating ion transport and water permeation. Experimental results revealed that reducing the AEM thickness led to a pronounced decline in ester production: at equivalent current densities, the FE$_{propyl\ acetate}$ decreased from 16.5% to 1.5% when the membrane thickness decreased from 100 to 40 μm (Fig. S19). Notably, no ester products were detected when employing the X37-50 Grade RT (50-micro-thick) AEM, despite its previously reported effectiveness for CORR.[33] This is attributed to increased water permeation through the thinner AEM, which promotes

competitive hydrolysis of ketene.[34] Moreover, even at comparable thicknesses, substantial variations in FE$_{propyl\ acetate}$ were observed among different AEMs, which might be attributed to differences in interfacial properties between the membrane and the catalyst (Fig. S19).

Mechanistic insights into the selective formation of propyl acetate

We previously proposed that esters are formed through the nucleophilic addition reaction of alcohols to ketene generated from CORR in a MEA.[7] This reaction pathway is further supported by our experimental observations (Fig. 3d and S16–S21). In the CO + n-propanol co-feeding experiment, the introduction of n-propanol leads to a pronounced increase in propyl acetate formation, accompanied by a marked decrease in ethyl acetate production. This trend indicates that ester formation requires a highly reactive C$_2$ intermediate that couples with the alcohol. Meanwhile, the significant decrease in acetate formation suggests that the reactive C$_2$ species is likely ketene, which is widely considered the key intermediate to acetate.[35–37] In the CO + H$_2$O co-feeding experiment, the FE of acetate increased while that of ester products decreased, showing a clear inverse relationship. This opposite trend further supports the presence of a ketene intermediate, as ketene is known to undergo rapid hydrolysis to acetate in water-rich environments rather than
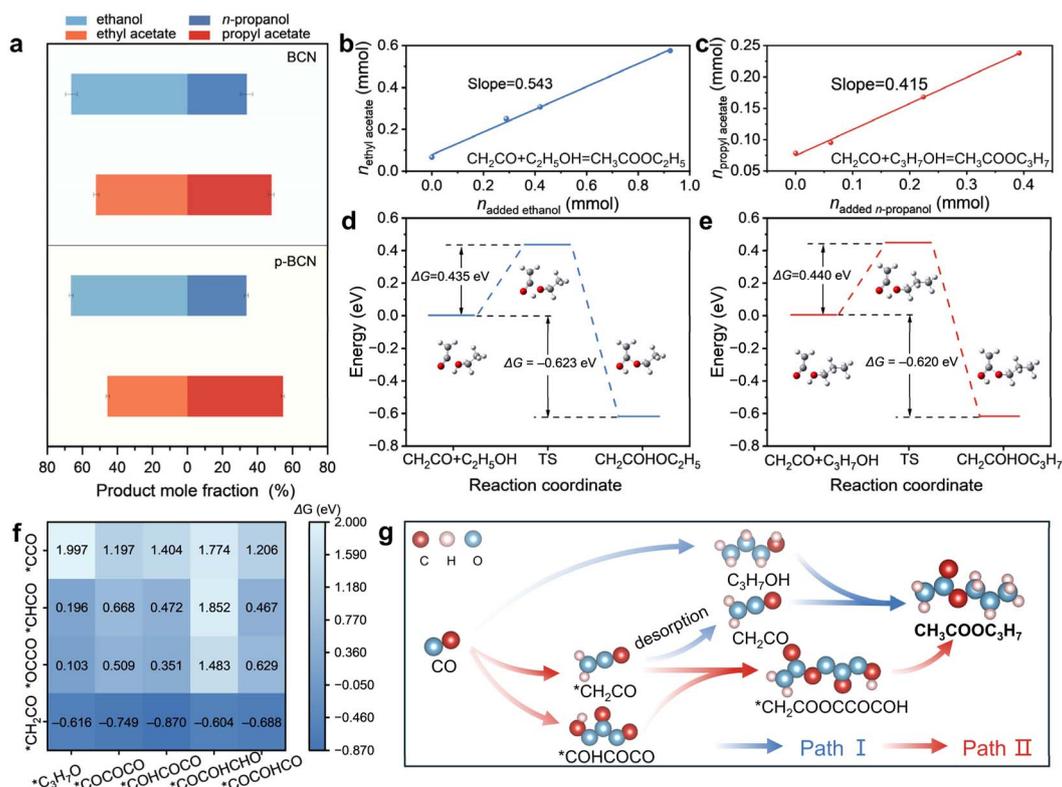

Fig. 4 Mechanistic investigation of propyl acetate formation. (a) Product distributions within alcohol and ester categories over BCN and p-BCN during CO electroreduction. (b and c) Dependence of ethyl acetate (b) and propyl acetate (c) formation rates on the concentration of ethanol and n-propanol feeds, respectively. (d and e) Calculated reaction energy profiles for ketene coupling with ethanol (d) and n-propanol (e). (f) Gibbs free energy changes for C$_2$–C$_3$ intermediate coupling. (g) Proposed reaction mechanisms for electrochemical formation of propyl acetate. Error bars correspond to the standard deviations of at least three independent measurements.

coupling with alcohols. Collectively, these results provide strong indirect evidence for the generation of ketene during CORR and its participation in coupling reactions with alcohols to form ester. Furthermore, this pathway implies a direct proportional relationship between alcohol generation and ester formation. However, propyl acetate constitutes up to 54.4% of the total esters produced, whereas n-propanol accounts for only 33.6% among the alcohol products over the p-BCN-derived catalyst. While, ethyl acetate accounted for only 45.5% even though ethanol makes up approximately 66.4% of the alcohol products. Similar conclusions can be inferred from the BCN data (Fig. 4a). The selectivity toward propyl acetate is significantly higher than expected based on the relative abundance of n-propanol, which challenges the current mechanistic understanding.

We studied the reactivity of n-propanol and ethanol toward ketene to understand the underlying mechanism. Varied amounts of ethanol and n-propanol were co-fed with CO into the MEA, respectively (Fig. 4b and c). There is a linear correlation between both the alcohol feed amounts and the ester yields. However, the slope for ethanol (0.543) was notably steeper than that for n-propanol (0.415), suggesting that ethanol reacts more readily with ketene than n-propanol. This

observation aligns with the Gaussian calculations, which indicate a slightly lower activation energy for the ethanol–ketene reaction (0.435 eV) compared to that of the n-propanol–ketene reaction (0.440 eV) (Fig. 4d, e and S22). Therefore, ethyl acetate forms more readily than propyl acetate when more ethanol is available if the ketene–alcohol nucleophilic addition pathway was the sole operative mechanism. However, our experimental results clearly indicate the opposite trend. Accordingly, we propose a C_2–C_3 intermediate coupling pathway for propyl acetate formation in addition to the ketene–alcohol nucleophilic addition reaction.

We performed DFT calculations to assess the plausibility of the proposed C_2–C_3 coupling pathway. Specifically, the coupling barriers for various C_2 and C_3 species on Cu-based surfaces were computed (Fig. 4f, S23–25 and Table S4). Among all combinations, the couplings of $^*CH_2CO$ to $^*COCOCO$, $^*COHCOCO$, and $^*COCOHCO$ to form a C_5 intermediate exhibited lower Gibbs free energy change than that of the reaction between ketene and n-propanol as well as ethanol, indicating that these pathways are thermodynamically favourable for propyl acetate formation (Fig. 4g).

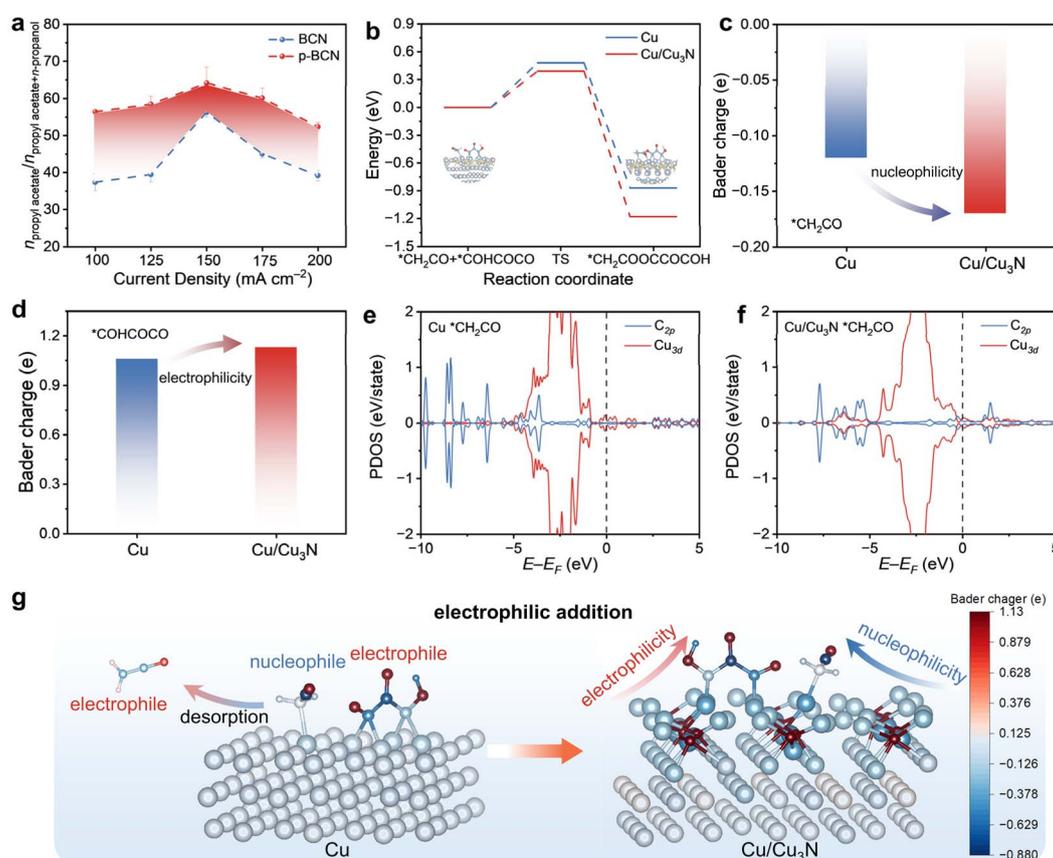We conducted DFT calculations on Cu and Cu/Cu_3N surfaces to gain further insight into the higher production of prolyl

Fig. 5 DFT elucidation of the intrinsic origin for enhanced propyl acetate formation. (a) Molar fraction of propyl acetate among C_3-containing products over BCN and p-BCN. (b) Reaction energy profiles for $^*CH_2CO$−$^*COHCOCO$ coupling on Cu and Cu/Cu_3N surfaces. (c and d) Bader charge of adsorbed $^*CH_2CO$ (c) and $^*COHCOCO$ (d) on Cu and Cu/Cu_3N surfaces. (e and f) PDOS of $^*CH_2CO$ on Cu (e) and Cu/Cu_3N (f). (g) Schematic illustration of the electronic structure modulation of $^*CH_2CO$ and $^*COHCOCO$ on Cu $vs.$ Cu/Cu_3N. Error bars correspond to the standard deviations of at least three independent measurements.

acetate on the p-BCN-derived catalyst than that on the BCN-derived catalyst (Fig. 5a). We took the C_2–C_3 coupling between key intermediates *CH_2CO and *COHCOCO having the lowest Gibbs energy change as an example. The coupling of *CH_2CO and *COHCOCO on Cu/Cu_3N is both thermodynamically and kinetically favourable than pure Cu (Fig. 5b and S26). Moreover, charge difference density maps reveal enhanced charge redistribution of the surface adsorbed species at the coupling site on Cu/Cu_3N, particularly at the Cu–N boundary (Fig. S27). This conclusion is further supported by Bader charge analysis. Notably, the *CH_2CO intermediate exhibits a greater negative charge on the Cu/Cu_3N surface ($-0.17\ e$) compared to Cu ($-0.12\ e$), reflecting an enhanced nucleophilic character. At the same time, *COHCOCO shows an increased positive charge ($+1.13\ e$ vs. $+1.04\ e$ on Cu), which strengthens the nucleophile–electrophile complementarity between *CH_2CO and *COHCOCO, facilitating their coupling via an electrophilic addition mechanism (Fig. 5c and d). Notably, this behaviour contrasts with the gas-phase reactivity of ketene, which typically acts as an electrophile in the nucleophilic addition with n-propanol (path I). Consequently, the Cu/Cu_3N interface not only stabilizes intermediates but also reverses the intrinsic electrophilic character of ketene, enabling an alternative coupling route (path II). PDOS analysis presents enhanced adsorbate–surface interactions between both *CH_2CO and *COHCOCO and the Cu/Cu_3N surface, providing more possibility for their further coupling (Fig. 5e, f and S28). Moreover, the Cu_{3d} states exhibit greater localization near the Fermi level in the presence of Cu_3N compared to those in pure Cu, resulting in enhanced surface electronic activity of Cu to promote the activation of intermediates and for efficient C–O bond formation. Collectively, these findings demonstrate that the Cu/Cu_3N interface creates an electronically optimized environment that promotes C_2–C_3 electrophilic addition through synergistic charge redistribution and orbital alignment (Fig. 5g). Such interfacial control over product selectivity underscores the critical role of electronic structure engineering in CO electroreduction.

We therefore propose that the predominant formation of propyl acetate in the current system results from both the alcohol–ketene nucleophilic addition reaction and, to a significant extent, electrophilic addition between surface-stabilized C_2 (*CH_2CO) and C_3 intermediates such as *COHCOCO. Specifically, the Cu/Cu_3N interface offers a conducive environment for C–C and C–O bond formation through the stabilization of reactive intermediates, enhancement of their spatial proximity, and improved charge transfer across the heterojunction. These synergistic effects reduce the energy barriers for electrophilic addition of C_2–C_3 intermediates, thereby enabling an efficient and selective catalytic pathway for propyl acetate production. This dual-pathway mechanism rationalizes the observed high selectivity toward propyl acetate.

Conclusions

In summary, we report the electrosynthesis of propyl acetate from CORR with considerable performance on a Cu/Cu_3N catalyst. Novel dual reaction pathways involving both alcohol–ketene nucleophilic addition reaction and electrophilic addition between surface-stabilized C_2 (*CH_2CO) and C_3 intermediates are proposed for the propyl acetate formation. The rationally designed Cu/Cu_3N interface promotes the formation, stabilization, and activation of key multi-carbon intermediates, thereby facilitating the electrophilic addition between C_2 and C_3 intermediates. Findings here not only provide a new one-step route in the selective electrosynthesis of esters from CO feedstocks, but also enrich theoretical insights into understanding the C–C and C–O coupling steps in the CO/CO_2RR process. Looking forward to the future, there remains considerable room for improvement in both the mechanistic understanding and performance of electrosynthesis of ester. On one hand, the molecular structure of acetate esters suggests that their formation involves multiple C–C and C–O coupling steps, which adds complexity to the elucidation of their reaction mechanisms. More comprehensive theoretical simulations, combined with complementary experimental validations, are essential for guiding the development of efficient catalysts and optimized reactor designs. On the other hand, ester production performance is significantly influenced by the type of AEM employed. Moreover, the knowledge gained from catalyst development and reactor configuration in CORR cannot be directly transferred to the electrosynthesis of esters. Therefore, the development of AEMs capable of establishing suitable local environments to stabilize key reaction intermediates, in conjunction with integrated reactor engineering and catalyst design, represents a critical research direction.

Author contributions

Y. Z. and S. W. supervised the project. Y. Z. and X. L. conceived the idea and designed the experiments. X. L. synthesized the samples, performed the electrochemical experiments and analyzed the results. X. L. and J. W. and Y. H. carried out the SEM, TEM, XPS and FTIR analysis. Y. J. carried out the simulations. W. C., Y. H, and Y. L. conducted the XAS measurements and assisted in analyzing the results. All authors discussed the results and assisted with the manuscript preparation.

Conflicts of interest

There are no conflicts to declare.

Data availability

The data supporting the findings of this study are available within the article and its supplementary information (SI). All other relevant source data are available from the corresponding authors upon reasonable request. Source data are provided with this paper.

Supplementary information is available. See DOI: https://doi.org/10.1039/d5sc08178e.

Acknowledgements

References

1 J. Y. T. Kim, C. Sellers, S. Hao, T. P. Senftle and H. Wang, Different distributions of multi-carbon products in CO_2 and CO electroreduction under practical reaction conditions, *Nat. Catal.*, 2023, **6**, 1115–1124.

2 Z. Li, X. Li, R. Wang, A. C. Mata, C. S. Gerke, S. Xiang, A. Mathur, L. Zhang, D.-Z. Lin, T. Li, K. N. Jayarapu, A. Liu, L. Gupta, A. I. Frenkel, V. Sara Thoi, P. M. Ajayan, S. Roy, Y. Liu and Y. Liu, Electro-activated indigos intensify ampere-level CO_2 reduction to CO on silver catalysts, *Nat. Commun.*, 2025, **16**, 3206.

3 S. Kwon, J. Zhang, R. Ganganahalli, S. Verma and B. S. Yeo, Enhanced carbon monoxide electroreduction to > 1 A cm^{-2} C_{2+} products using copper catalysts dispersed on MgAl layered double hydroxide nanosheet house-of-cards scaffolds, *Angew. Chem., Int. Ed.*, 2023, **135**, e202217252.

4 ChemAnalyst, *N-Propyl Acetate Market Analysis: Plant Capacity, Production, Operating Efficiency, Technology, Demand & Supply, End-User Industries, Distribution Channel, Regional Demand*, 2021, https://www.chemanalyst.com/industry-report/n-propyl-acetate-market-612.

5 Market Research Future. *Propyl Acetate Market Size, Share & Analysis Report 2034*, 2025, https://www.marketresearchfuture.com/reports/propyl-acetate-market-22750.

6 G. Mitran and O. D. Pavel, Mechanisms & Catalysis. Kinetics of acetic acid esterification with propanol in the presence of supported molybdena catalysts, *React. Kinet. Mech. Catal.*, 2015, **114**, 197–209.

7 Y. Zhou, R. Ganganahalli, S. Verma, H. R. Tan and B. S. Yeo, Production of C_3-C_6 acetate esters via CO electroreduction in a membrane electrode assembly cell, *Angew. Chem., Int. Ed.*, 2022, **61**, e202202859.

8 H. Zhang, D. Raciti and A. Hall, Disordered interfacial H_2O promotes electrochemical C-C coupling, *Nat. Chem.*, 2025, 1–8.

9 Z. Wu, X. Zhang, P. Yang, Z. Niu, F. Gao, Y. Zhang, L. Chi, S. Sun, J. D. Mu, P. Lu, Y. Li and M. Gao, Gerhardtite as a precursor to an efficient CO-to-acetate electroreduction catalyst, *J. Am. Chem. Soc.*, 2023, **145**, 24338–24348.

10 J. Liu, O. Peng, D. Chen, X. Han, S. Xi, Q. Hu, Z. Gao, Y. Yuan, K. Zhang and K. P. Loh, Asymmetric C-C coupling to drive CO Conversion to acetate, *J. Am. Chem. Soc.*, 2025, **147**, 24932–24940.

11 F. Zhang, N. Cao, C. Wang, S. Wang, Y. He, Y. Shi, M. Yan, Y. Bao, Z. Li and P. Xie, In situ stabilization of Cu^+ for CO_2 electroreduction via environmental-molecules-induced ZnO_{1-x} shield, *Nat. Commun.*, 2025, **16**, 6082.

12 K. Yue, Y. Qin, H. Huang, Z. Lv, M. Cai, Y. Su, F. Huang and Y. Yan, Stabilized Cu^0-Cu^{1+} dual sites in a cyanamide framework for selective CO_2 electroreduction to ethylene, *Nat. Commun.*, 2024, **15**, 7820.

13 S. Lee, D. Kim and J. Lee, Electrocatalytic production of C_3-C_4 compounds by conversion of CO_2 on a chloride-induced biphasic Cu_2O-Cu catalyst, *Angew. Chem., Int. Ed.*, 2015, **54**, 14701–14705.

14 Z. Jiang, C. Clavaguéra, S. A. Denisov, J. Ma and M. Mostafavi, Role of oxide-derived Cu on the initial elementary reaction intermediate during catalytic CO_2 reduction, *J. Am. Chem. Soc.*, 2024, **146**, 30164–30173.

15 Y. Zhou, F. Che, M. Liu, C. Zou, Z. Liang, P. D. Luna, H. Yuan, J. Li, Z. Wang, H. Xie, H. Li, P. Chen, E. Bladt, R. Quintero-Bermudez, T. Sham, S. Bals, J. Hofkens, D. Sinton, G. Chen and E. H. Sargent, Dopant-induced electron localization drives CO_2 reduction to C_2 hydrocarbons, *Nat. Chem.*, 2018, **10**, 974–980.

16 Z. Yin, C. Yu, Z. Zhao, X. Guo, M. Shen, N. Li, M. Muzzio, J. Li, H. Liu, H. Lin, J. Yin, G. Lu, D. Su and S. Sun, Cu_3N nanocubes for selective electrochemical reduction of CO_2 to ethylene, *Nano Lett.*, 2019, **19**, 8658–8663.

17 X. Zhang, J. Chen, G. Gao, H. Wang, Y. Tang, B. Sun, Y. Ni, Y. Chen and Y. P. Feng, The activity origin of CN-Cu electrocatalysts for ethanol formation in the CO_2 reduction reaction under working conditions, *J. Mater. Chem. A*, 2024, **12**, 3580–3588.

18 Z. Liang, T. Zhuang, A. Seifitokaldani, J. Li, C. Huang, C. Tan, Y. Li, P. D. Luna, C. T. Dinh, Y. Hu, Q. Xiao, P. Hsieh, Y. Wang, F. Li, R. Quintero-Bermudez, Y. Zhou, P. Chen, Y. Pang, S. Lo, L. Chen, H. Tan, Z. Xu, S. Zhao, D. Sinton and E. H. Sargent, Copper-on-nitride enhances the stable electrosynthesis of multi-carbon products from CO_2, *Nat. Commun.*, 2018, **9**, 3828.

19 W. Niu, J. Feng, J. Chen, L. Deng, W. Guo, H. Li, L. Zhang, Y. Li and B. Zhang, High-efficiency C_3 electrosynthesis on a lattice-strain-stabilized nitrogen-doped Cu surface, *Nat. Commun.*, 2024, **15**, 7070.

20 H. Xiao, W. A. Goddard III, T. Cheng and Y. Liu, Cu metal embedded in oxidized matrix catalyst to promote CO_2 activation and CO dimerization for electrochemical reduction of CO_2, *Proc. Natl. Acad. Sci. U. S. A.*, 2017, **114**, 6685–6688.

21 N. Ba, L. Zhu, H. Li, G. Zhang, J. Li and J. Sun, 3D rod-like copper oxide with nanowire hierarchical structure: Ultrasound assisted synthesis from $Cu_2(OH)_3NO_3$ precursor, optical properties and formation mechanism, *Solid State Sci.*, 2016, **53**, 23–29.

22 H. Shi, H. Luo, L. Li, Y. Li, T. Zhang, Z. Liu, J. Cui, L. Gu, L. Zhang, Y. Hu, H. Li and C. Li, Stabilizing Cu^+ species in

Cu₂O/CuO catalyst via carbon intermediate confinement for selective CO₂RR, *Adv. Funct. Mater.*, 2024, **34**, 2310913.

23 M. Zheng, P. Wang, X. Zhi, K. Yang, Y. Jiao, J. Duan, Y. Zheng and S. Z. Qiao, Electrocatalytic CO₂-to-C₂₊ with ampere-level current on heteroatom-engineered copper via tuning *CO intermediate coverage, *J. Am. Chem. Soc.*, 2022, **144**, 14936–14944.

24 L. Zhao, Q. Sun, M. Li, Y. Zhong, P. Shen, Y. Lin and K. Xu, Antiperovskite nitride Cu₃N nanosheets for efficient electrochemical oxidation of methanol to formate, *Sci. China Mater.*, 2023, **66**, 1820–1828.

25 L. Cheng, D. He, X. Ma, H. Deng, Y. Ruan, R. Sun, L. Tian, H. Zhou, J. Chen, X. Wang, H. Pan, W. Guo and Y. Wu, A 2D porous Cu₃N catalyst for efficient CO electroreduction to multicarbon products at an ampere level current density, *Adv. Funct. Mater.*, 2024, **34**, 2406056.

26 K. Mavridou, M. Zervos, F. Pinakidou, M. Brzhezinskaya and M. Katsikini, Oxidation of Cu₃N thin films obtained from Cu annealed under NH₃:O₂ flow: A Raman and N-K-edge NEXAFS study, *J. Alloys Compd.*, 2022, **914**, 165293.

27 J. Li, Y. Chen, B. Yao, W. Yang, X. Cui, H. Liu, S. Dai, S. Xi, Z. Sun, W. Chen, Y. Qin, J. Wang, Q. He, C. Ling, D. Wang and Z. Zhang, Cascade dual sites modulate local CO coverage and hydrogen-binding strength to boost CO₂ electroreduction to ethylene, *J. Am. Chem. Soc.*, 2024, **146**, 5693–5701.

28 Z. Zhang, X. Feng, Z. Zhang, L. Chen, W. Liu, L. Tong, X. Gao and J. Zhang, Graphdiyne enabled nitrogen vacancy formation in copper nitride for efficient ammonia synthesis, *J. Am. Chem. Soc.*, 2024, **146**, 14898–14904.

29 Z. Wei, W. Wang, T. Shao, S. Yang, C. Liu, D. Si, R. Cao and M. Cao, Constructing Ag/Cu₂O interface for efficient neutral CO₂ electroreduction to C₂H₄, *Angew. Chem., Int. Ed.*, 2025, **64**, e202417066.

30 Y. Qu, K. Yang, W. Li, G. Wang, L. Xiao, G. Wang and L. Zhuang, Operando diagnosis of MEA-Type CO₂ electrolyzer via distribution of relaxation times analysis, *ACS Energy Lett.*, 2024, **9**, 3042–3048.

31 Y. Sun, F. Bai, J. Liu, S. Sun, Y. Mao, X. Liu, Y. Huang and Y. Chen, Identification of degradation reasons for a CO₂ MEA electrolyzer using the distribution of relaxation times analysis, *J. Phys. Chem. Lett.*, 2024, **15**, 9122–9128.

32 X. Wang, P. Ou, A. Ozden, S. Hung, J. n Tam, C. M. Gabardo, J. Y. Howe, J. Sisler, K. Bertens, F. P. García de Arquer, R. K. Miao, C. P. O'Brien, Z. Wang, J. Abed, A. S. Rasouli, M. Sun, A. H. Ip, D. Sinton and E. H. Sargent, Efficient electrosynthesis of *n*-propanol from carbon monoxide using a Ag-Ru-Cu catalyst, *Nat. Energy*, 2022, **7**, 170–176.

33 Q. Xu, S. Garg, A. B. Moss, M. Mirolo, I. Chorkendorff, J. Drnec and B. Seger, Identifying and alleviating the durability challenges in membrane-electrode-assembly devices for high-rate CO electrolysis, *Nat. Catal.*, 2023, **6**, 1042–1051.

34 W. Luc, X. Fu, J. Shi, J. Lv, M. Jouny, B. H. Ko, Y. Xu, Q. Tu, X. Hu, J. Wu, Q. Yue, Y. Liu, F. Jiao and Y. Kang, Two-dimensional copper nanosheets for electrochemical reduction of carbon monoxide to acetate, *Nat. Catal.*, 2019, **2**, 423–430.

35 H. H. Heenen, H. Shin, G. Kastlunger, S. Overa, J. A. Gauthier, F. Jiao and K. Chan, The mechanism for acetate formation in electrochemical CO₍₂₎ reduction on Cu: selectivity with potential, pH, and nanostructuring, *Energy Environ. Sci.*, 2022, **15**, 3978–3990.

36 Y. Ji, Z. Chen, R. Wei, C. Yang, Y. Wang, J. Xu, H. Zhang, A. Guan, J. Chen, T. Sham, J. Luo, Y. Yang, X. Xu and G. Zheng, Selective CO-to-acetate electroreduction via intermediate adsorption tuning on ordered Cu–Pd sites, *Nat. Catal.*, 2022, **5**(4), 251–258.

37 L. Zhang, J. Feng, R. Wang, L. Wu, X. Song, X. Jin, X. Tan, S. Jia, X. Ma, L. Jing, Q. Zhu, X. Kang, J. Zhang, X. Sun and B. Han, Switching CO-to-acetate electroreduction on Cu atomic ensembles, *J. Am. Chem. Soc.*, 2024, **147**(1), 713–724.